

GrapHist: Graph Self-Supervised Learning for Histopathology

Sevda Ögüt^{a,*}, Cédric Vincent-Cuaz^a, Natalia Dubljevic^{a,1}, Carlos Hurtado^{a,1}, Vaishnavi Subramanian^a, Pascal Frossard^a, Dorina Thanou^a

^a*LTS4, EPFL, Lausanne, 1015, Vaud, Switzerland*

Abstract

Self-supervised vision models have achieved notable success in digital pathology. However, their domain-agnostic transformer architectures are not originally designed to account for fundamental biological elements of histopathology images, namely cells and their complex interactions. In this work, we hypothesize that a biologically-informed modeling of tissues as cell graphs offers a more efficient representation learning. Thus, we introduce **GrapHist**, a novel **graph**-based self-supervised learning framework for **histopathology**, which learns generalizable and structurally-informed embeddings that enable diverse downstream tasks. GrapHist integrates masked autoencoders and heterophilic graph neural networks that are explicitly designed to capture the heterogeneity of tumor microenvironments. We pre-train GrapHist on a large collection of 11 million cell graphs derived from breast tissues and evaluate its transferability across in- and out-of-domain benchmarks. Our results show that GrapHist achieves competitive performance compared to its vision-based counterparts in slide-, region-, and cell-level tasks, while requiring four times fewer parameters. It also drastically outperforms fully-supervised graph models on cancer subtyping tasks. Finally, we also release five graph-based digital pathology datasets used in our study at <https://huggingface.co/ogutsevda/datasets>, establishing the first large-scale graph benchmark in this field. Our code is available at <https://github.com/ogutsevda/graphist>.

*Corresponding author

Email address: `sevda.ogut@epfl.ch` (Sevda Ögüt)

¹Work done during student project at LTS4.

Keywords: graph representation learning, digital pathology, self-supervised learning

1. Introduction

Recent advances in large-scale self-supervised learning (SSL) have led to promising vision foundation models for digital pathology, addressing clinically relevant tasks such as cancer typing and grading, treatment response assessment, and survival prediction [1, 2, 3]. These models analyze high-resolution pan-cancer whole-slide images (WSIs), with significant heterogeneity across different biological scales. Traditionally, they operate on small patches of 224×224 pixels extracted from WSIs. Each patch is encoded using vision transformers, which divide it into non-overlapping regions of 14×14 pixels, referred to as tokens [4]. However, since these tokens are defined by a regular image grid, they are not typically aligned with cells, whose morphology and spatial organization are the core biological entities examined by pathologists for diagnostic and prognostic decisions [5, 6]. While grid-based tokens can capture low-level visual patterns, they are not natively tailored to recognize cell interactions, which are highly relevant in biological systems. This raises a fundamental question: **What constitutes a proper representation for the development of AI models in digital pathology?**

In this work, we postulate that explicitly modeling individual cells and their spatial arrangement using graphs yields a more efficient general-purpose representation learning paradigm than conventional domain-agnostic vision approaches. Consequently, we introduce **GrpHist**, the first **graph**-based self-supervised learning framework for **histopathology** that learns context-aware cell-level representations via large-scale pre-training. In GrpHist, each cell is represented as a node characterized by discriminative features of shape, color intensity, and texture, while edges are defined based on spatial proximity. GrpHist learns generalizable embeddings through a self-supervised pre-training strategy, using masked autoencoding of cell graphs following the GraphMAE framework [7]. In this setting, subsets of node features are masked and then reconstructed from their local neighborhoods. Since the interactions arising from diverse cell types within tissues and especially within the tumor microenvironment (TME) are inherently heterogeneous [8], we incorporate heterophilic Graph Neural Networks (GNNs) [9] in both the encoder and decoder of GrpHist. This formulation is highly

flexible as it remains agnostic to the actual staining technique and applies to digital pathology images of arbitrary size.

We pre-train GrapHist on a large-scale dataset of 11 million cell graphs derived from breast tissues. The nodes of these graphs are detected using a lightweight cell segmentation model [10], ensuring that the pre-processing step is computationally inexpensive. We compare GrapHist against well-established vision backbones used in digital pathology foundation models, namely DINOv2 [11] and MAE [12], which we pre-train from scratch on the same data to ensure a fair comparison of the representations. Following pre-training, we evaluate the learned representations across a diverse suite of downstream tasks. GrapHist achieves better zero-shot performance on slide- and region-level tumor subtyping, patient survival analysis, as well as cell classification tasks, while requiring four times fewer parameters, making it an efficient alternative. This indicates that representing tissues through their core biological components provides an effective inductive bias, particularly in cell-rich regions, retaining the essential information while significantly reducing dimensionality. Moreover, we benchmark GrapHist against fully-supervised graph baselines to evaluate the efficacy of self-supervised pre-training. Our experiments demonstrate that GrapHist achieves substantial improvements—up to 40 percentage points—on slide- and region-level tasks. Moreover, while fully supervised baselines remain stronger on cell-level tasks with abundant annotations, GrapHist consistently outperforms them in low-supervision regimes. These results highlight GrapHist’s zero-shot effectiveness when supervision is scarce relative to the task complexity. Finally, we publicly release our five graph-based digital pathology datasets to foster further research progress in histopathology. These datasets enrich existing images with graph representations. Note that they also constitute a resource for the graph learning community, which suffers from a lack of large-scale, real-world datasets [13]. Our main contributions are as follows:

- We introduce GrapHist, the first large-scale graph-based self-supervised learning framework for histopathology, which explicitly models complex dependencies between cells in the tissue through masked autoencoding with heterophilic GNNs.
- We demonstrate that GrapHist achieves competitive yet more parameter- and compute-efficient performance compared to popular vision-based self-supervised learning approaches for tumor subtyping, survival analysis, and cell classification tasks.

- We introduce and publicly release a collection of five graph datasets to encourage future research in graph representation learning for digital pathology.

Overall, our findings show that GrapHist establishes a new paradigm in self-supervised learning for histopathology, offering compact, biologically grounded, and spatially-aware representations through graph-based modeling, paving the way for more knowledge-driven digital pathology foundation models.

2. Related Work

2.1. Foundation Models for Digital Pathology

While the rise of vision foundation models prompted their application in digital pathology, their pre-training on natural images resulted in a significant domain gap that hindered effective generalization [3]. Consequently, the field has leaned toward building domain-specific foundation models, including CTransPath [1], GigaPath [14], Virchow [15], and UNI [3], to name a few. A comprehensive benchmarking of such models is provided in [16]. These models are typically trained on billions of pathology image patches from private databases using large vision transformers, often in conjunction with self-supervised learning frameworks such as DINOv2 [11]. Yet, their grid-based architectures lack an inherent inductive bias for cells and their interactions, namely the primary biological entities guiding pathologists’ reasoning. This limitation forces the models to implicitly learn these structures from raw pixels, thereby impeding their learning efficiency. To improve the latter, our work explores a paradigm shift based on biologically-informed graphs, which are agnostic to the staining technique.

2.2. Graphs in Histopathology

In this vein, a growing body of research has focused on abstracting histopathology images into cell graphs and leveraging graph machine learning to analyze cellular organization and interactions. GRAPE-Net [17] utilizes graph convolutional blocks to retain spatial relationships and represents each image patch as a node for lung tumor stratification. OCDPI [18] proposes to use a graph attention network and min-cut pooling for treatment response prediction in ovarian cancer patients. HACT-Net [19] hierarchically builds a

cell-to-tissue graph and examines it with cell- and tissue-level GNNs. Similarly, Pina et al. model WSIs with cell- and region-level graphs and employ graph clustering techniques for region of interest (RoI) detection [20]. We refer the interested reader to the survey from [21] for a detailed explanation of GNNs in histopathology and remark that these methods are often trained on task-specific, limited-size datasets. However, the potential of large-scale, self-supervised pre-training on cell graphs for developing graph-based models remains largely unexplored.

2.3. Graph Self-Supervised Learning

Self-supervision has become a popular learning paradigm for graph data as it extracts informative knowledge without relying on manual labels through well-designed pretext tasks [22]. Graph SSL methods typically fall under two categories: contrastive and generative. Contrastive learning approaches, such as GRACE [23] and GraphCL [24], learn representations by maximizing the agreement between different augmented views of the same graph (positive pairs) while minimizing disagreement with views of different graphs (negative pairs). Generative methods like GraphMAE [7] adopt a reconstruction objective, training the model to predict masked node features or structural information from the surrounding context. These methods are currently among the most competitive in the graph literature and have therefore inspired our study. However, they typically rely on standard message-passing backbones that assume graph homophily, where connected nodes share similar features. This assumption is ill-suited for histopathology, where the TME is inherently heterophilic, driven by complex interactions between diverse entities such as tumor, immune, and stromal cells. To bridge this gap, in the next Section, we propose integrating heterophilic GNNs into a masked autoencoding framework.

3. Self-Supervised Graph Learning for Digital Pathology

Current vision models rely on grid-based representations that obscure the underlying spatial biology, whereas existing graph-based models remain task-specific and lack general-purpose applicability. Moreover, the heterogeneous nature of the TME challenges the standard graph-based models, which assume homophilic neighborhood structures. To address these limitations, we introduce GrapHist, a graph-based self-supervised learning framework that models biological tissues as cell graphs via masked autoencoding and captures

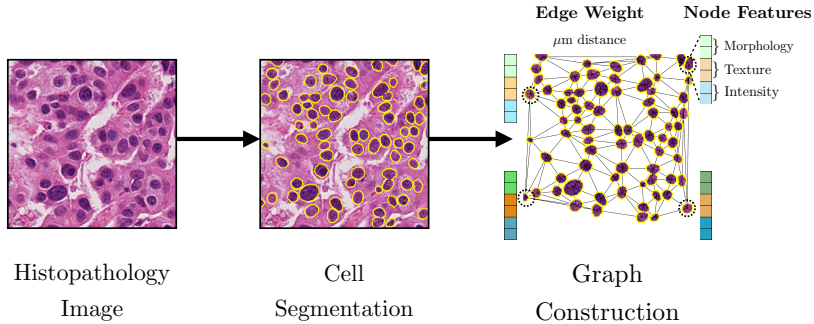


Figure 1: **Pre-processing steps in GrapHist.** Individual cells are segmented within a digital pathology image. These cells and their spatial arrangement are then converted into a graph. Each cell is a node with morphology, texture, and intensity descriptors. Edges connect neighboring cells and are weighted by their geographic distance. Best viewed in color.

complex cellular dependencies with heterophilic GNNs. In the following, we present the building blocks of GrapHist.

3.1. From Histopathology Images to Cell Graphs

Whole-slide images are giga-pixel resolution scans of digitized biopsies, typically stained with Haematoxylin and Eosin (H&E). Similar to [19], we transform these images into cell graphs to explicitly capture the cellular composition and spatial arrangement, following the procedure detailed in Figure 1. Specifically, we first perform cell segmentation using the state-of-the-art StarDist model with a U-Net backbone [10] at a patch- or region-level to identify individual cells. This step discards the surrounding tissue, yielding a cell-centric representation that focuses learning on cellular morphology and spatial organization. Then, we model the image as an undirected cell graph $\mathcal{G} = (\mathcal{V}, \mathcal{E})$, where \mathcal{V} denotes its set of n nodes and \mathcal{E} its set of edges. The nodes $\{v_i\}_{i \in [n]} \in \mathcal{V}$ corresponding to cells are further endowed with features $\mathbf{X} = (\mathbf{x}_i) \in \mathbb{R}^{n \times 96}$, detailed in Table B.6 of the Appendix, describing cells’ morphology, texture, and color intensities, that are known to be discriminant across cell and tissue types [25, 26]. The edges model the relative spatial arrangement of cells and are computed via Delaunay triangulation [27, 28]. Furthermore, edges connecting two cells more than $100 \mu\text{m}$ [29] apart are removed in order to emphasize plausible physical interactions. Finally, each edge $(v_i, v_j) \in \mathcal{E}$ is weighted by the Euclidean distance $a_{ij} \in (0, 100)$ in μm ,

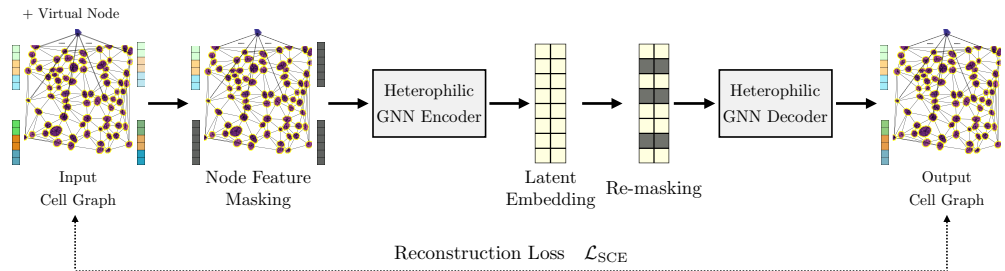


Figure 2: **Pre-training of GraphHist.** We add a virtual node that is connected to all other nodes in the input cell graph and adopt a masked autoencoding strategy, where a subset of input node features is randomly masked. A GNN-based encoder–decoder architecture is then trained to recover the original node features, decoding from a re-masked version of the latent embeddings.

between connected cells v_i and v_j , summarized in a *sparse* adjacency matrix $\mathbf{A} = (a_{ij}) \in \mathbb{R}^{n \times n}$.

3.2. Masked Graph Autoencoding with Heterophilic GNNs

The core principle of GraphHist is graph-based self-supervision that combines masked node feature reconstruction with heterophilic message passing to learn representations of spatial cellular organization. We next describe the main components of our framework and illustrate it in Figure 2.

Self-Supervised Framework. GraphHist leverages the GraphMAE framework [7]. Specifically, we randomly mask the features of a subset of nodes $\tilde{\mathcal{V}} \subset \mathcal{V}$ in the input graph. This masking procedure comes down to replacing observed node features either by a learnable vector or a randomly sampled node feature in the graph. A GNN-based encoder then learns latent embeddings from this corrupted graph. During decoding, the previously masked nodes are re-masked, and a GNN-based decoder is trained to reconstruct their original features \mathbf{x}_i from the learned embeddings \mathbf{h}_i . The objective is to minimize the scaled cosine error defined as follows, where the scaling factor $\gamma \geq 1$ is adopted from [7] to down-weight the contribution of easy samples:

$$\mathcal{L}_{\text{SCE}} = \frac{1}{|\tilde{\mathcal{V}}|} \sum_{v_i \in \tilde{\mathcal{V}}} \left(1 - \frac{\mathbf{x}_i^\top \mathbf{h}_i}{\|\mathbf{x}_i\| \cdot \|\mathbf{h}_i\|} \right)^\gamma. \quad (1)$$

Capturing Tumor Heterogeneity. In contrast to the homophilic GNNs used in vanilla GraphMAE for encoding and decoding, we propose using heterophilic GNNs, which are better suited to the inherent heterogeneity of tumor microenvironments. Particularly, we utilize the Adaptive Channel Mixing (ACM) architecture [9], with channels derived from the random walk matrix $\mathbf{A}_{rw} = \mathbf{D}^{-1}\mathbf{A}$, where \mathbf{D} is the degree matrix. At each layer, the ACM block processes input graphs through three distinct channels: a low-pass $\mathbf{A}_L = (\mathbf{I} + \mathbf{A}_{rw})/2$, a high-pass $\mathbf{A}_H = (\mathbf{I} - \mathbf{A}_{rw})/2$, and a neutral channel $\mathbf{A}_I = \mathbf{I}$, where $\mathbf{I} \in \mathbb{R}^{n \times n}$ is the identity matrix. We denote the node feature matrix of layer k as $\mathbf{H}^{(k)}$, with $\mathbf{H}^{(0)} = \mathbf{X}$. Formally, the update rule for the k^{th} layer in the ACM architecture is given below for $c \in \{L, H, I\}$:

$$\mathbf{H}^{(k)} = \sum_{c \in \{L, H, I\}} \alpha_c^{(k)} \mathbf{H}_c^{(k)} \quad \text{where} \quad \begin{cases} \alpha_c^{(k)} = \text{Softmax}\left(\frac{\hat{\alpha}_c^{(k)} \mathbf{W}_{\text{mix}}^{(k)}}{T}\right), \\ \hat{\alpha}_c^{(k)} = \text{Sigmoid}(\mathbf{H}_c^{(k)} \mathbf{W}_c^{(k)}), \\ \mathbf{H}_c^{(k)} = \text{MLP}_c^{(k)}(\mathbf{A}_c \mathbf{H}^{(k-1)}), \end{cases} \quad (2)$$

with the weights $\mathbf{W}_c^{(k)} \in \mathbb{R}^{d \times d}$, hidden dimension d , temperature parameter $T \in \mathbb{R}^+$, and the mixing matrix $\mathbf{W}_{\text{mix}}^{(k)} \in \mathbb{R}^{3 \times 3}$ applied across channels. Our model learns an adaptive convex combination of channel-specific embeddings that responds to the local histopathological context. This enables it to smooth signals within homogeneous tissue regions, sharpen representations at heterotypic boundaries such as tumor–stroma interfaces, and preserve cell-specific features when neighborhood aggregation is uninformative.

Improving Expressivity. We enhance the model’s representational capacity with two mechanisms. First, to better encode long-range dependencies within graphs, we introduce a virtual node connected to all nodes in each graph [30, 31]. The virtual node’s features are zero-initialized, and its edge weights are set to the mean of all edge weights in the pre-training dataset. Second, to improve information flow across layers and prevent oversmoothing, we employ a jumping knowledge strategy [32]. This mechanism acts as a residual connection by concatenating the outputs from each layer, followed by a linear projection to a fixed dimension d . This yields GrapHist’s final node embeddings $\mathbf{H} \in \mathbb{R}^{n \times d}$.

Algorithm 1 summarizes the full pre-processing and self-supervised pre-training pipeline of GrapHist. Overall, GrapHist’s sparse cell graph design

Algorithm 1: The GrapHist Framework

Input: Histopathology dataset \mathcal{D}_I .

Output: Pre-trained encoder \mathcal{F}_θ .

Pre-processing:

foreach *image* $I \in \mathcal{D}_I$ **do**

 Perform cell segmentation on I with StarDist [10].

 Extract cell-level features as detailed in Table B.6.

 Construct edges between cells using Delaunay triangulation.

 Obtain a cell graph $\mathcal{G} = (\mathcal{V}, \mathcal{E})$.

Store the graph-based dataset in \mathcal{D}_G .

Pre-training:

for *epoch* = 1 **to** 100 **do**

 Sample a batch of graphs $\{\mathcal{G}\} \subset \mathcal{D}_G$.

 Enrich them with virtual nodes.

foreach *graph* \mathcal{G} **do**

 Sample a subset of nodes $\tilde{\mathcal{V}} \subset \mathcal{V}$.

 Mask their features with probability r_m .

 Randomly replace masked features with probability r_r .

 Encode the graph using a heterophilic GNN (Eq. 2).

 Re-mask the same nodes in $\tilde{\mathcal{V}}$.

 Decode the graph with a single-layer heterophilic GNN (Eq. 2).

 Compute the reconstruction loss \mathcal{L}_{SCE} (Eq. 1).

 Update encoder and decoder parameters via backpropagation.

return \mathcal{F}_θ

	# Slides	# Patches	Avg # Nodes	Avg # Edges	# Classes
Slide-level					
TCGA-BRCA [33]	998	11 149 500	43.94	119.16	2
Region-level					
BACH [34]	394	14 341	35.05	92.93	4
BRACS [35]	4493	96 153	46.96	128.09	7
BreakHis [36]	522	709	17.26	41.43	2
Cell-level					
PanNuke [37]	—	7215	22.66	57.16	5
NuCLS (main/super) [38]	—	1694	30.76	78.62	7/4

Table 1: Statistics for the graph-based slide-, region-, and cell-level datasets.

and message passing GNN architecture enable the encoding of tissues with a computational complexity that is *linear* in the number of cells. This positions GrapHist as a memory-efficient approach, unlike vision transformer models commonly used in digital pathology, whose complexity is *quadratic* in the number of tokens, which is roughly four times the number of cells at a standard magnification of $20\times$, as seen in Table 1. Note that histopathology slides can encompass millions of cells per slide.

3.3. Deriving Cell, Region, and Slide-Level Embeddings

Following Algorithm 1, we pre-train GrapHist using a large dataset of cell graphs, yielding context-aware cell-level embeddings. This enables our framework to operate across biological scales. In other words, we can directly utilize the produced node embeddings $\mathbf{H} \in \mathbb{R}^{n \times d}$ for cell-level tasks, such as cell type identification. We can also aggregate them into a region-level embedding $\mathbf{h} \in \mathbb{R}^d$, taken as the mean of cell embeddings in the following, to address localized tumor subtyping tasks. Finally, the derived region embeddings can be further aggregated into slide-level ones by employing standard attention-based multiple instance learning (MIL) approaches, commonly used in digital pathology [39]. In particular, we consider the best performing method among the three state-of-the-art attention-based MIL approaches, namely ABMIL [40], additive ABMIL [41], and conjunctive ABMIL [42], which mainly differ in how they couple the attention mechanism with a classifier. More formally,

they compute the slide logits \mathbf{s}_i as follows:

$$\underbrace{\mathbf{s}_i = g\left(\sum_{j=1}^{K_i} a_{ij} \mathbf{h}_{ij}\right)}_{\text{(ABMIL)}}, \quad \underbrace{\mathbf{s}_i = \sum_{j=1}^{K_i} g(a_{ij} \mathbf{h}_{ij})}_{\text{(add-ABMIL)}}, \quad \underbrace{\mathbf{s}_i = \sum_{j=1}^{K_i} a_{ij} g(\mathbf{h}_{ij})}_{\text{(conj-ABMIL)}}$$

where $\{\mathbf{h}_{ij}\}_{j \in [K_i]}$ are the K_i patch embeddings of the slide i , $g(\cdot)$ is a classifier, and each attention coefficient a_{ij} is defined as $\exp(\mathbf{w}^\top \tanh(\mathbf{V} \mathbf{h}_{ij}^\top)) / \sum_{k=1}^{K_i} \exp(\mathbf{w}^\top \tanh(\mathbf{V} \mathbf{h}_{ik}^\top))$ with \mathbf{w} and \mathbf{V} as learnable parameters. Thus, pre-training GrapHist to learn cell embeddings enables multi-scale representations of the tissue, spanning cells, regions, and whole slides.

4. Experiment Design

In the following, we detail our experimental framework to assess the empirical benefits of GrapHist in comparison to state-of-the-art vision-based self-supervised approaches and fully-supervised graph methods.

4.1. Datasets

Common tasks associated with H&E datasets require operating on large WSIs or the RoIs they contain. To process these, we first employ the approach of [43] to segment tissue regions from their background. Then, unless otherwise specified, we adopt standard pre-processing conventions used in digital pathology foundation models, which consist of rescaling the segmented images at $20\times$ magnification (i.e., $0.5 \mu\text{m}/\text{pixel}$) before patching them into non-overlapping 224×224 -pixel tiles.

For self-supervised pre-training, we utilize a dataset of 998 H&E-stained breast cancer WSIs from the TCGA database [33], comprising about 11 million 224×224 -pixel patches. This dataset is also used for an in-domain (ID) evaluation task involving the classification of infiltrating ductal carcinoma and lobular carcinoma across different grades, as well as survival analysis.

For downstream generalization, we evaluate on five out-of-domain (OOD) datasets spanning diverse tissue types and two different biological scales, detailed in Appendix A. Grouped by task granularity, the evaluation includes three region-level datasets—BACH [34], BRACS [35], and BreakHis [36]—which focus on breast cancer subtyping, and two cell-level datasets—PanNuke [37] and NuCLS [38]—targeting cell phenotype identification. We

assess models on PanNuke at both $20\times$ and $40\times$ magnification, considering all pan-cancer tissues, and only the breast cancer ones, which are closer to our pre-training distribution. For NuCLS, we treat its two tasks separately, including respectively fine-grained cell labels and a coarser super grouping. For all these image-based datasets, we construct their graph-based counterparts using the methodology described in Section 3.1 and report their statistics in Table 1. A discussion of pre-processing runtimes is given in Appendix C.

4.2. Self-Supervised Baselines

To quantify the benefits of incorporating prior biological knowledge through cell graphs, we compare GrapHist against widely used self-supervised vision models, namely DINOv2 [11] and MAE [12]. In practice, DINOv2, which builds on self-distillation using a student-teacher pair of vision transformers, is nowadays one of the most utilized approaches [44]. In addition, earlier masked autoencoding frameworks such as MAE remain competitive and are often preferred for generative tasks [45].

To ensure a fair comparison, we pre-train DINOv2 and MAE from scratch on patch-level images from TCGA-BRCA, whereas GrapHist is pre-trained with graphs generated from the same patches, all for 100 epochs using a batch size of 2048. We employ a ViT-S/16 backbone for our vision-based models [4], adopting the standard hyperparameters provided by the authors as they are well-validated for various data scales and architectures. However, due to the lack of large-scale benchmarks for the GraphMAE framework used in GrapHist, we validated its key hyperparameters following guidelines from [7], including the embedding dimension in $\{512, 768, 1024\}$, the masking ratio (r_m) in $\{0.50, 0.75\}$, and the replacement ratio (r_r) in $\{0.00, 0.10\}$. We set the encoder and decoder depths to 5 and 1, respectively, following the approach of Hou et al. for large datasets.

Once these SSL models are pre-trained, we systematically consider the CLS token of the vision transformers and the mean of the cell embeddings of GrapHist’s encoder as patch embeddings for WSI- and RoI-level tasks. For cell-level tasks, GrapHist directly provides cell embeddings through its node representations. In contrast, vision-based SSL baselines do not explicitly model cells, as they operate on fixed-grid tokens that are misaligned with irregular cellular boundaries. To enable a fair zero-shot comparison, we therefore compute cell embeddings for these models as convex combinations of patch tokens that spatially overlap each nucleus, using the corresponding

segmentation masks. Finally, we evaluate these frozen representations by applying non-linear probing for cell-level tasks and utilizing the attention-based MIL aggregators (Section 3.3) for region- and slide-level benchmarks.

4.3. Supervised Baselines

To isolate the benefits of our self-supervised pre-training and hand-crafted feature design, we benchmark GrapHist against two fully supervised graph baselines, which are trained end-to-end directly on the downstream task labels, i.e., slide, region, or cell classes, for each specific dataset. Both baselines employ a similar heterophilic GNN backbone as GrapHist but differ in their input node features:

- **ACM-bio:** This model operates on exactly the same attributed graphs as GrapHist and aims at quantifying the benefit of large-scale self-supervised pre-training over task-specific supervised learning.
- **ACM-UNI:** To evaluate the efficacy of our hand-crafted cell descriptors, we substitute them in graphs used by GrapHist and ACM-bio, with high-dimensional deep features derived from UNI [3], a well-established vision foundation model for histopathology. Specifically, for each segmented cell (typically 20×20 pixels), we resize the corresponding image to 224×224 pixels and compute the corresponding UNI embedding.

For both supervised methods, we faced significant overfitting issues while using similar hyperparameters to the ACM backbone of GrapHist, hence we validated its hyperparameters in different ranges, as detailed in Appendix C, depending on the type of tasks.

5. Results

5.1. WSI-level Analysis

We first compare the performance of GrapHist with the aforementioned baselines on the in-domain WSI dataset of TCGA-BRCA in two downstream tasks, namely breast cancer subtyping and survival analysis.

Model	Datasets			
	WSI	RoI		
	TCGA-BRCA	BACH	BRACS	BreakHis
Supervised graph models				
ACM-bio	OOM	38.37 ± 2.16	21.55 ± 2.62	55.82 ± 10.33
ACM-UNI	OOM	29.03 ± 9.92	19.95 ± 3.27	76.27 ± 9.23
Self-supervised vision models				
DINOv2	62.43 ± 1.75	<u>59.25 ± 3.34</u>	52.68 ± 1.78	83.44 ± 2.25
MAE	<u>66.72 ± 1.27</u>	57.94 ± 3.91	<u>56.33 ± 0.76</u>	<u>87.74 ± 1.66</u>
Ours				
GrapHist	72.25 ± 1.40	69.16 ± 3.37	60.30 ± 0.46	89.37 ± 1.94

Table 2: Test macro F1 scores (%) on WSI and RoI-level breast cancer tumor subtyping tasks. For each dataset and model, we report the best MIL aggregation variant. Best and second-best results are highlighted in bold and underlined, respectively.

5.1.1. Tumor Subtyping

We evaluate slide-level breast tumor subtyping on TCGA-BRCA, particularly the classification of infiltrating ductal carcinoma versus invasive lobular carcinoma. We utilize the best performing MIL method introduced in Section 3.3 to aggregate patch-level representations from pre-trained models to classify the full slide. Additionally, we validate a range of hyperparameters using a 5-fold stratified cross-validation with a held-out test set, with further details in Appendix C. We report the test macro F1 performance in Table 2 and remark that GrapHist significantly outperforms the best self-supervised vision baseline by a margin of 5.5%. Furthermore, GrapHist demonstrates superior memory scalability compared to fully supervised graph methods, which are trained end-to-end and require storing all patch-level graphs of a slide simultaneously for backpropagation, leading to prohibitive memory costs (OOM).

5.1.2. Survival Analysis

We evaluate the prognostic value of the learned embeddings on TCGA-BRCA by performing survival analysis, i.e., Kaplan-Meier [46] and Cox analysis [47]. Following [48], for each patient, we first compute a patient-level embedding by averaging their WSI embeddings, themselves defined as the mean of patch embeddings obtained directly from pre-trained models. Overall survival time is defined as days-to-death for deceased patients and days-

to-last-follow-up for censored patients, with the event indicator set to 1 for death and 0 otherwise. As typical in survival analysis, we then fit a penalized Cox proportional hazards model using the patient embeddings as covariates, compute risk scores, and stratify patients into high- and low-risk groups based on the median risk score. Group separation is assessed using Kaplan–Meier curves and log-rank tests. As shown in Figure 3, GrapHist achieves more pronounced risk-group separation compared to vision-based baselines. We report the concordance index (C-index), which measures the model’s ability to correctly rank patient risk (higher is better), and the p-value, which quantifies the statistical significance of the stratification. As seen in Table 3, GrapHist achieves the strongest performance, followed by MAE, while DINOv2 is consistently weaker, indicating the structure-aware benefit of our approach.

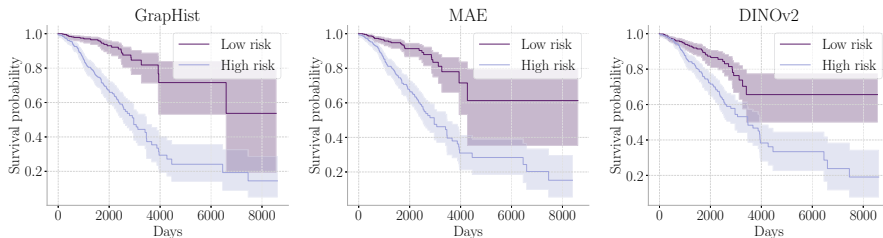


Figure 3: Kaplan-Meier curves with Cox risk groups.

Model	C-index	p-value
DINOv2	0.63	9.80×10^{-6}
MAE	0.72	1.54×10^{-13}
GrapHist	0.76	1.29×10^{-15}

Table 3: Survival analysis on TCGA-BRCA.

5.1.3. Computational Efficiency

We stress that the high performance of GrapHist is achieved at a significantly lower computational cost than that of DINOv2 and MAE. As detailed in Table 4, GrapHist contains between 2 to 5 times fewer parameters than its ViT-based competitors. Moreover, it was pre-trained 3 to 7 times faster than the used vision transformers, whose computational efficiency is drastically

increased with FlashAttention [49]. These results align with our theoretical complexity analysis in Section 3.2, stating GrapHist as nearly linear in the number of cells, as opposed to vision transformers, which are quadratic in the number of tokens. This efficiency is empirically confirmed by the inference metrics in Table 4. GrapHist reduces peak GPU memory usage by over 50% and accelerates processing speed (mean ms/patch) by a factor of 4 compared to the baselines.

Model	Pre-training		Inference	
	# Params (10^6)	Time (h)	Peak GPU mem (GB)	Mean ms/patch
DINOv2	22.01	180	0.380	0.885
MAE	47.58	350	0.309	1.053
GrapHist	9.50	50	0.142	0.221

Table 4: Pre-training and inference efficiency on an NVIDIA A100 GPU. Pre-training time is measured on TCGA-BRCA. Inference metrics are measured with BACH.

5.2. RoI-level Analysis

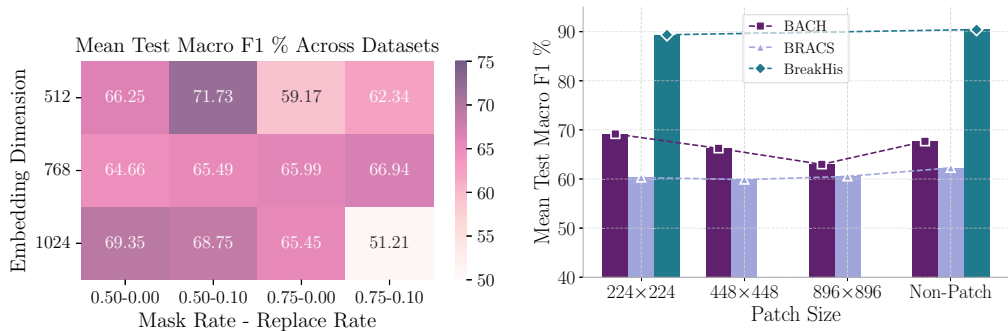
We next benchmark the performance of GrapHist on the OOD datasets of BACH, BRACS, and BreakHis on tumor subtyping and also demonstrate the generalization of our model across various patch sizes. We follow the same setup as in Section 5.1 with further implementation details in Appendix C.

5.2.1. Tumor Subtyping

As seen in Table 2, GrapHist outperforms all competitors on the three RoI benchmarks, surpassing the self-supervised vision baselines by margins of up to 9.9%. These results demonstrate the ability of our approach to generalize across different breast cancer types, grades, and clinical centers. In contrast, fully-supervised graph methods perform significantly worse on these tasks, potentially due to their tendency to overfit to limited downstream labels. This highlights the transferability of our self-supervised framework.

5.2.2. Sensitivity Analysis

We study the sensitivity of GrapHist to its validated hyperparameters on the out-of-distribution RoI benchmarks. For each configuration, we report the test macro F1 performance achieved on average across MIL variants in Figure 4a. We can observe a notable performance gap of 8-20% between



(a) Mean test macro F1 scores across OOD RoI-level tasks of various hyperparameter configurations. (b) Mean test macro F1 comparison across patch sizes in OOD RoI-level tasks.

Figure 4: Quantitative results of sensitivity analysis and patch size robustness.

the tested configurations. Nonetheless, the overall hyperparameter sensitivity dynamics are consistent with findings of [7], even though we operate at a significantly larger scale than their setting. Our best performing model coincides with the lowest masking rate and the highest replacement rate as seen in Figure 4a. The best embedding dimension matches several molecular datasets whose graphs have around a hundred continuous node features [7].

5.2.3. Patch Size Robustness

To demonstrate the agnosticism of our framework to input patch sizes, we evaluate GrapHist, which was pre-trained on 224×224 pixel patches, on larger inputs without any retraining for the RoI datasets. Notably, we construct graphs and compute embeddings for patches with pixel widths of 224, 448, and 896, and conduct the MIL evaluation described above. We also perform non-linear probing on the full RoI images, going up to about 4000×4000 pixels for the BRACS dataset. Notice that certain RoI images on BreakHis are too small to go higher than 448×448 pixel patches. Interestingly, we observe in Figure 4b that the performance for BRACS and BreakHis remains remarkably stable across all patch sizes, including those on the non-patched image. Consequently, we can construct a single graph for an entire region of interest, without sacrificing performance. This allows us to bypass patching and MIL aggregation entirely in RoI settings, resulting in a simpler inference pipeline that is easier to deploy.

Model	PanNuke 20×		PanNuke 40×		NuCLS	
	Breast	PanCancer	Breast	PanCancer	main	super
Supervised graph models						
ACM-bio	<u>56.61 ± 0.31</u>	<u>62.73 ± 0.02</u>	57.06 ± 0.33	<u>65.80 ± 0.11</u>	22.13 ± 1.59	37.35 ± 1.30
ACM-UNI	58.05 ± 0.03	67.63 ± 0.66	<u>56.81 ± 0.18</u>	66.99 ± 0.80	21.68 ± 1.03	39.46 ± 1.33
Self-supervised vision models						
DINOv2	54.82 ± 0.48	50.49 ± 0.37	53.86 ± 0.54	49.27 ± 0.42	21.42 ± 1.49	41.17 ± 2.26
MAE	47.71 ± 0.64	54.88 ± 0.55	47.54 ± 0.58	55.26 ± 0.12	<u>25.19 ± 3.14</u>	<u>45.31 ± 1.05</u>
Ours						
GraphHist	55.26 ± 0.30	58.78 ± 0.15	56.43 ± 0.04	59.47 ± 0.11	26.57 ± 2.16	46.24 ± 3.89

Table 5: Test macro F1 scores (%) on cell-level type identification tasks for all the evaluated models.

5.3. Cell-level Analysis

To directly assess whether GraphHist learns useful cell-centric representations, we finally experiment on cell type identification tasks detailed in Section 4.1 derived from the PanNuke and NuCLS datasets. For SSL methods, cell embeddings (see Section 4.2) are directly classified by non-linear probing using folds provided with the datasets. Test macro F1 scores are reported in Table 5. Strikingly, we observe that GraphHist consistently outperforms self-supervised vision baselines across all six experimental settings. Against fully supervised graph baselines, we observe that performance is largely dictated by domain alignment and the amount of labeled cells. On the NuCLS dataset, which contains several images from TCGA-BRCA, GraphHist achieves the highest performance. Conversely, supervised models excel on the PanNuke dataset, particularly in the pan-cancer setting, as they benefit from direct supervision on diverse tissue types unseen by our model. However, this performance gap narrows significantly on the breast-only subset of PanNuke, indicating that the disparity is primarily due to the domain shift.

6. Discussion

In this work, we introduced GraphHist, a graph-based self-supervised learning framework that utilizes cell graphs as a biologically meaningful inductive bias for histopathology data. Pre-trained on a large-scale corpus of breast tissue, GraphHist learns compact, low-dimensional embeddings that effectively encode critical spatial and cellular details. When benchmarked against vision transformers of comparable size, our model demonstrates that structured representations can achieve competitive, and often superior, downstream performance in tumor subtyping, survival analysis, and phenotype identification

tasks. We also release five new digital pathology graph datasets, establishing the first benchmark of its kind. Overall, our framework not only opens new research avenues in histopathology but also signals a paradigm shift: purely pixel-based vision models can be replaced by graph-based approaches that combine efficiency with inherent biological relevance.

However, we acknowledge that our framework has certain limitations. First, the process of distilling images into graphs currently discards the extracellular matrix (ECM). As the ECM may contain relevant biological signals, especially for downstream tasks involving non-cancerous tissues, future work will aim to incorporate this information while maintaining a linear time complexity with respect to the number of nodes. Second, our model is currently trained on a limited corpus of breast tissues and scaling the dataset to encompass pan-cancer cohorts represents a promising direction for improving generalizability. This is corroborated by our cell-level experiments, which also advocate investigating parameter-efficient fine-tuning approaches to further enhance GrapHist embeddings in settings where extensive cell annotations are available [50]. Beyond these limitations, we believe that GrapHist is a flexible framework and opens avenues for future research. Since the graph construction relies on cells and their shape descriptors, our method can be easily extended to diverse imaging modalities, such as immunohistochemistry or immunofluorescence, via domain alignment, fine-tuning, or simply pre-training from scratch. Finally, our cell-centric approach provides grounds for early multi-modal fusion, as node features can be augmented with single-cell molecular information before pre-training.

7. Acknowledgements

The authors would like to thank LTS4 members for their valuable feedback and acknowledge the Research Computing Platform (RCP) at EPFL for providing computational resources.

References

- [1] X. Wang, S. Yang, J. Zhang, M. Wang, J. Zhang, W. Yang, J. Huang, X. Han, Transformer-based unsupervised contrastive learning for histopathological image classification, *Medical Image Analysis* 81 (2022) 102559.
- [2] A. Filiot, R. Ghermi, A. Olivier, P. Jacob, L. Fidon, A. M. Kain, C. Sallard, J.-B. Schiratti, Scaling self-supervised learning for histopathology with masked image modeling, *medRxiv* (2023).
- [3] R. J. Chen, T. Ding, M. Y. Lu, D. F. Williamson, G. Jaume, A. H. Song, B. Chen, A. Zhang, D. Shao, M. Shaban, Towards a general-purpose foundation model for computational pathology, *Nature Medicine* (2024).
- [4] A. Dosovitskiy, L. Beyer, A. Kolesnikov, D. Weissenborn, X. Zhai, T. Unterthiner, M. Dehghani, M. Minderer, G. Heigold, S. Gelly, J. Uszkoreit, N. Houlsby, An image is worth 16x16 words: Transformers for image recognition at scale, in: *ICLR*, 2021.
- [5] S. Shafi, A. V. Parwani, Artificial intelligence in diagnostic pathology, *Diagnostic Pathology* 18 (1) (2023) 109.
- [6] R. J. Chen, C. Chen, Y. Li, T. Y. Chen, A. D. Trister, R. G. Krishnan, F. Mahmood, Scaling vision transformers to gigapixel images via hierarchical self-supervised learning, in: *IEEE CVPR*, 2022, pp. 16144–16155.
- [7] Z. Hou, X. Liu, Y. Cen, Y. Dong, H. Yang, C. Wang, J. Tang, Graphmae: Self-supervised masked graph autoencoders, in: *ACM SIGKDD*, 2022, pp. 594–604.
- [8] N. M. Anderson, M. C. Simon, The tumor microenvironment, *Current biology* 30 (16) (2020) R921–R925.
- [9] S. Luan, C. Hua, Q. Lu, J. Zhu, M. Zhao, S. Zhang, X.-W. Chang, D. Precup, Revisiting heterophily for graph neural networks, in: *NeurIPS*, 2022, pp. 1362–1375.
- [10] U. Schmidt, M. Weigert, C. Broaddus, G. Myers, Cell detection with star-convex polygons, in: *MICCAI*, 2018, pp. 265–273.

- [11] M. Oquab, T. Darcet, T. Moutakanni, H. V. Vo, M. Szafraniec, V. Khalidov, P. Fernandez, D. HAZIZA, F. Massa, A. El-Nouby, M. Assran, N. Ballas, W. Galuba, R. Howes, P.-Y. Huang, S.-W. Li, I. Misra, M. Rabbat, V. Sharma, G. Synnaeve, H. Xu, H. Jegou, J. Mairal, P. Labatut, A. Joulin, P. Bojanowski, DINOv2: Learning robust visual features without supervision, TMLR (2024).
- [12] K. He, X. Chen, S. Xie, Y. Li, P. Dollár, R. Girshick, Masked autoencoders are scalable vision learners, in: IEEE CVPR, 2022, pp. 16000–16009.
- [13] M. Bechler-Speicher, B. Finkelshtein, F. Frasca, L. Müller, J. Tönshoff, A. Siraudin, V. Zaverkin, M. M. Bronstein, M. Niepert, B. Perozzi, et al., Position: Graph learning will lose relevance due to poor benchmarks, in: ICML, 2025.
- [14] H. Xu, N. Usuyama, J. Bagga, S. Zhang, R. Rao, T. Naumann, C. Wong, Z. Gero, J. González, Y. Gu, A whole-slide foundation model for digital pathology from real-world data, *Nature* 630 (8015) (2024) 181–188.
- [15] E. Vorontsov, A. Bozkurt, A. Casson, G. Shaikovski, M. Zelechowski, K. Severson, E. Zimmermann, J. Hall, N. Tenenholtz, N. Fusi, A foundation model for clinical-grade computational pathology and rare cancers detection, *Nature Medicine* 30 (10) (2024) 2924–2935.
- [16] P. Neidlinger, O. S. El Nahhas, H. S. Muti, T. Lenz, M. Hoffmeister, H. Brenner, M. van Treeck, R. Langer, B. Dislich, H. M. Behrens, et al., Benchmarking foundation models as feature extractors for weakly supervised computational pathology, *Nature Biomedical Engineering* (2025) 1–11.
- [17] R. H. Gindra, Y. Zheng, E. J. Green, M. E. Reid, S. A. Mazzilli, D. T. Merrick, E. J. Burks, V. B. Kolachalama, J. E. Beane, Graph perceiver network for lung tumor and bronchial premalignant lesion stratification from histopathology, *The American Journal of Pathology* 194 (7) (2024) 1285–1293.
- [18] Z. Yang, Y. Zhang, L. Zhuo, K. Sun, F. Meng, M. Zhou, J. Sun, Prediction of prognosis and treatment response in ovarian cancer patients

from histopathology images using graph deep learning: a multicenter retrospective study, *European Journal of Cancer* 199 (2024) 113532.

- [19] P. Pati, G. Jaume, A. Foncubierta-Rodriguez, F. Feroce, A. M. Anniello, G. Scognamiglio, N. Brancati, M. Fiche, E. Dubruc, D. Riccio, Hierarchical graph representations in digital pathology, *Medical Image Analysis* 75 (2022) 102264.
- [20] O. Pina, V. Vilaplana, Self-supervised graph representations of wsis, in: *Geometric Deep Learning in Medical Image Analysis*, 2022, pp. 107–117.
- [21] S. Brussee, G. Buzzanca, A. M. Schrader, J. Kers, Graph neural networks in histopathology: Emerging trends and future directions, *Medical Image Analysis* (2025) 103444.
- [22] Y. Liu, M. Jin, S. Pan, C. Zhou, Y. Zheng, F. Xia, P. S. Yu, Graph self-supervised learning: A survey, *IEEE Transactions on Knowledge and Data Engineering* 35 (6) (2022) 5879–5900.
- [23] Y. Zhu, Y. Xu, F. Yu, Q. Liu, S. Wu, L. Wang, Deep graph contrastive representation learning, *arXiv preprint arXiv:2006.04131* (2020).
- [24] Y. You, T. Chen, Y. Sui, T. Chen, Z. Wang, Y. Shen, Graph contrastive learning with augmentations, in: *NeurIPS*, 2020, pp. 5812–5823.
- [25] S. Zhao, D.-P. Chen, T. Fu, J.-C. Yang, D. Ma, X.-Z. Zhu, X.-X. Wang, Y.-P. Jiao, X. Jin, Y. Xiao, Single-cell morphological and topological atlas reveals the ecosystem diversity of human breast cancer, *Nature Communications* 14 (1) (2023) 6796.
- [26] L. Fournier, G. Haefliger, A. Vernhes, V. Jung, I. Letovanec, P. Frossard, C. Vincent-Cuaz, R. Luisier, Extended pre-training of histopathology foundation models uncovers co-existing breast cancer archetypes characterized by rna splicing or $\text{tgf-}\beta$ dysregulation, *bioRxiv* (2025).
- [27] Y. S. Elshakhs, K. M. Deliparaschos, T. Charalambous, G. Oliva, A. Zolotas, A comprehensive survey on delaunay triangulation: applications, algorithms, and implementations over cpus, gpus, and fpgas, *IEEE Access* 12 (2024) 12562–12585.

- [28] Y. Zhou, S. Graham, N. Alemi Koohbanani, M. Shaban, P.-A. Heng, N. Rajpoot, Cgc-net: Cell graph convolutional network for grading of colorectal cancer histology images, in: IEEE CVPR, 2019.
- [29] K. Francis, B. O. Palsson, Effective intercellular communication distances are determined by the relative time constants for cyto/chemokine secretion and diffusion, PNAS 94 (23) (1997) 12258–12262.
- [30] J. Gilmer, S. S. Schoenholz, P. F. Riley, O. Vinyals, G. E. Dahl, Neural message passing for quantum chemistry, in: ICML, 2017, pp. 1263–1272.
- [31] J. Southern, F. D. Giovanni, M. M. Bronstein, J. F. Lutzeyer, Understanding virtual nodes: Oversquashing and node heterogeneity, in: ICLR, 2025.
- [32] K. Xu, C. Li, Y. Tian, T. Sonobe, K.-i. Kawarabayashi, S. Jegelka, Representation learning on graphs with jumping knowledge networks, in: ICML, 2018, pp. 5453–5462.
- [33] J. N. Weinstein, E. A. Collisson, G. B. Mills, K. R. Shaw, B. A. Ozenberger, K. Ellrott, I. Shmulevich, C. Sander, J. M. Stuart, The cancer genome atlas pan-cancer analysis project, Nature Genetics 45 (10) (2013) 1113–1120.
- [34] G. Aresta, T. Araújo, S. Kwok, S. S. Chennamsetty, M. Safwan, V. Alex, B. Marami, M. Prastawa, M. Chan, M. Donovan, Bach: Grand challenge on breast cancer histology images, Medical Image Analysis 56 (2019) 122–139.
- [35] N. Brancati, A. M. Anniciello, P. Pati, D. Riccio, G. Scognamiglio, G. Jaume, G. De Pietro, M. Di Bonito, A. Foncubierta, G. Botti, Bracs: A dataset for breast carcinoma subtyping in h&e histology images, Database 2022 (2022).
- [36] F. A. Spanhol, L. S. Oliveira, C. Petitjean, L. Heutte, A dataset for breast cancer histopathological image classification, IEEE Biomedical Engineering 63 (7) (2015) 1455–1462.
- [37] J. Gamper, N. A. Koohbanani, K. Benes, S. Graham, M. Jahanifar, S. A. Khurram, A. Azam, K. Hewitt, N. Rajpoot, Pannuke dataset extension, insights and baselines, arXiv preprint arXiv:2003.10778 (2020).

- [38] M. Amgad, L. A. Atteya, H. Hussein, K. H. Mohammed, E. Hafiz, M. A. T. Elsebaie, A. M. Alhousseiny, M. A. AlMoslemany, A. M. Elmatboly, P. A. Pappalardo, R. A. Sakr, P. Mobadersany, A. Rachid, A. M. Saad, A. M. Alkashash, I. A. Ruhban, A. Alrefai, N. M. Elgazar, A. Abdulkarim, A.-A. Farag, A. Etman, A. G. Elsaeed, Y. Alagha, Y. A. Amer, A. M. Raslan, M. K. Nadim, M. A. T. Elsebaie, A. Ayad, L. E. Hanna, A. Gadallah, M. Elkady, B. Drumheller, D. Jaye, D. Manthey, D. A. Gutman, H. Elfandy, L. A. D. Cooper, Nucls: A scalable crowdsourcing approach and dataset for nucleus classification and segmentation in breast cancer, *GigaScience* 11 (2022).
- [39] M. Gadermayr, M. Tschuchnig, Multiple instance learning for digital pathology: A review of the state-of-the-art, limitations & future potential, *Computerized Medical Imaging and Graphics* 112 (2024) 102337.
- [40] M. Ilse, J. Tomczak, M. Welling, Attention-based deep multiple instance learning, in: *ICML, 2018*, pp. 2127–2136.
- [41] S. A. Javed, D. Juyal, H. Padigela, A. Taylor-Weiner, L. Yu, A. Prakash, Additive mil: Intrinsically interpretable multiple instance learning for pathology, in: *NeurIPS, 2022*, pp. 20689–20702.
- [42] J. Early, G. Cheung, K. Cutajar, H. Xie, J. Kandola, N. Twomey, Inherently interpretable time series classification via multiple instance learning, in: *ICLR, 2024*.
- [43] G. Campanella, M. G. Hanna, L. Geneslaw, A. Miraflor, V. Werneck Krauss Silva, K. J. Busam, E. Brogi, V. E. Reuter, D. S. Klimstra, T. J. Fuchs, Clinical-grade computational pathology using weakly supervised deep learning on whole slide images, *Nature Medicine* 25 (8) (2019) 1301–1309.
- [44] G. Campanella, C. Vanderbilt, T. Fuchs, Computational pathology at health system scale – self-supervised foundation models from billions of images, in: *AAAI Spring Symposium on Clinical Foundation Models, 2024*.
- [45] O. Kraus, K. Kenyon-Dean, S. Saberian, M. Fallah, P. McLean, J. Leung, V. Sharma, A. Khan, J. Balakrishnan, S. Celik, Masked autoencoders for microscopy are scalable learners of cellular biology, in: *IEEE CVPR, 2024*, pp. 11757–11768.

- [46] E. L. Kaplan, P. Meier, Nonparametric estimation from incomplete observations, *Journal of the American statistical association* 53 (282) (1958) 457–481.
- [47] D. R. Cox, Regression models and life-tables, *Journal of the Royal Statistical Society: Series B (Methodological)* 34 (2) (1972) 187–202.
- [48] E. Wulczyn, D. F. Steiner, Z. Xu, A. Sadhwani, H. Wang, I. Flament-Auvigne, C. H. Mermel, P.-H. C. Chen, Y. Liu, M. C. Stumpe, Deep learning-based survival prediction for multiple cancer types using histopathology images, *PloS one* 15 (6) (2020) e0233678.
- [49] T. Dao, D. Fu, S. Ermon, A. Rudra, C. Ré, Flashattention: Fast and memory-efficient exact attention with io-awareness, in: *NeurIPS*, 2022.
- [50] S. Li, X. Han, J. Bai, Adaptergnn: Parameter-efficient fine-tuning improves generalization in gnns, in: *AAAI*, Vol. 38, 2024, pp. 13600–13608.
- [51] D. Zhang, G. Lu, A comparative study on shape retrieval using fourier descriptors with different shape signatures, in: *ICIMADE*, 2001, pp. 1–9.
- [52] V. Vadori, A. Peruffo, J.-M. Graïe, L. Finos, E. Grisan, Automated classification of cell shapes: A comparative evaluation of shape descriptors, in: *IEEE ISBI*, 2025, pp. 1–4.

Appendix A. Dataset Details

Here, we provide details of the original image datasets. All patches are extracted at $20\times$ magnification and have a size of 224×224 pixels. The label distribution for each dataset is reported below.

Appendix A.1. Slide-level Tasks

TCGA-BRCA. We leverage this breast invasive carcinoma dataset, which comprises 1126 H&E-stained WSIs, sized up to $100K\times 100K$ pixels [33]. We obtain approximately 11 million patches from this dataset that serve two purposes in our study: (1) self-supervised pre-training to learn vision and graph representations, and (2) in-domain downstream evaluation corresponding to the classification of infiltrating ductal carcinoma and lobular carcinoma of different grades. Note that multiple other subtypes were excluded in this study due to their small sample size.

Appendix A.2. Region-level Tasks

BACH. We use this breast cancer histology dataset [34] of 400 RoI images for out-of-domain downstream evaluation. The pre-trained model embeddings are used for a four-class classification task of cancer subtyping distributed as normal, benign, in situ carcinoma, and invasive carcinoma.

BRACS. Similarly, we use this breast cancer dataset put forth by [35] of 4539 labeled RoIs for downstream evaluation. The end task consists of a seven-class classification of tumor subtypes, distributed as normal, pathological benign, usual ductal hyperplasia, flat epithelial atypia, atypical ductal hyperplasia, ductal carcinoma in situ, and invasive carcinoma.

BreakHis. The final region-level out-of-domain setting contains a dataset of 1995 labeled microscopic images of breast tumor tissue collected from 82 patients [36]. The downstream task is a binary classification of tumor type, with the labels of benign and malignant.

Appendix A.3. Cell-level Tasks

PanNuke. This cell-level dataset contains 200K annotated nuclei from 7904 patches and spans 19 distinct tissue types [37]. The end task provides granular classifications for nuclei into five categories of neoplastic, inflammatory, connective tissue, dead, and epithelial. We use the predefined three folds.

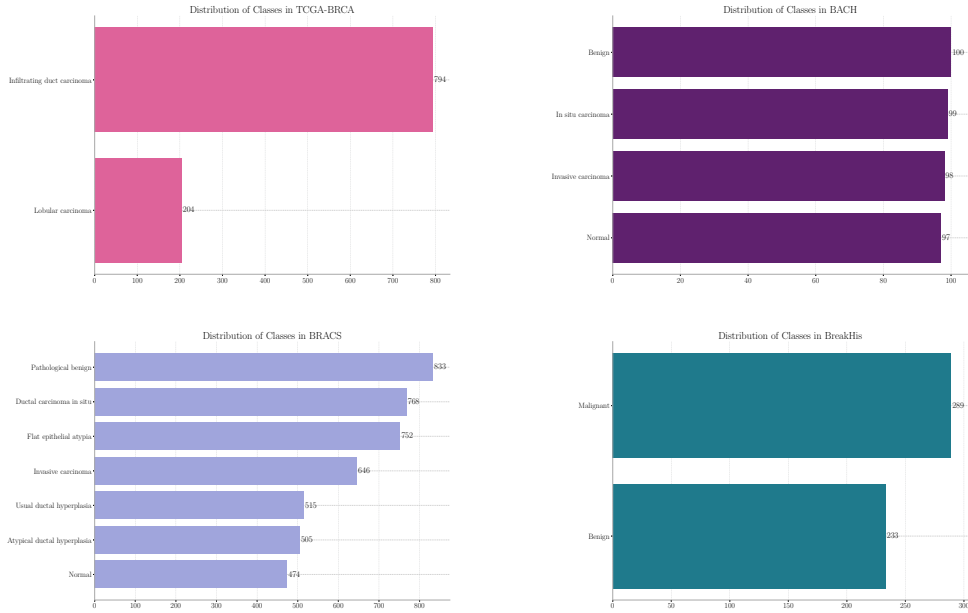


Figure A.5: Class label distributions of slide- and region-level datasets.

NuCLS. Finally, this dataset consists of over 220K annotated nuclei designed for three classification tasks [38]. The labels are organized into raw, main, and super sets, which represent varying levels of detail. The raw one features 13 fine-grained classes, while the main and super sets provide categorizations of 7 and 4 classes, respectively, by aggregating the more detailed labels into broader groups. We use only the main and super sets in this study.

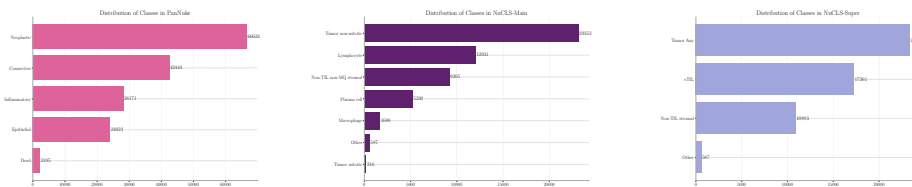


Figure A.6: Class label distributions of cell-level datasets.

Appendix B. Cell-level Features

We use the features shown in Table B.6 as node attributes for our cell graphs. Please refer to [51] for a detailed explanation of Fourier features with centroid signature and to [52] for their use as cell shape descriptors.

Nuclei-Color	Nuclei-Morph	Nuclei-Texture
min intensity R	probability	mean ASM
min intensity G	orientation	mean contrast
min intensity B	axis major length	mean correlation
max intensity R	axis minor length	mean dissimilarity
max intensity G	eccentricity	mean energy
max intensity B	area	mean homogeneity
mean intensity R	perimeter	std ASM
mean intensity G	circularity	std contrast
mean intensity B	elongation	std correlation
std intensity R	solidity	std dissimilarity
std intensity G	extent	std energy
std intensity B	Fourier descriptor 20	std homogeneity
skew intensity R	Fourier descriptor 30	skew ASM
skew intensity G		skew contrast
skew intensity B		skew correlation
kurtosis intensity R		skew dissimilarity
kurtosis intensity G		skew energy
kurtosis intensity B		skew homogeneity
mean intensity gray scale		kurtosis ASM
std intensity gray scale		kurtosis contrast
skew intensity gray scale		kurtosis correlation
kurtosis intensity gray scale		kurtosis dissimilarity
min intensity gray scale		kurtosis energy
max intensity gray scale		kurtosis homogeneity
		min ASM
		min contrast
		min correlation
		min dissimilarity
		min energy
		min homogeneity
		max ASM
		max contrast
		max correlation
		max dissimilarity
		max energy
		max homogeneity

Table B.6: The set of cell-level color, morphology, and texture descriptors used as input node features in our graph construction pipeline. R, G, and B stand for red, green, and blue, respectively.

Appendix C. Implementation Details

All experiments were run on NVIDIA A100 (80GB) and H200 (140GB) GPUs and the number of parameters in DINOv2, MAE, and GrapHist models can be found in the Table C.7. We provide the specific setup used in the *evaluation* of our self-supervised and fully-supervised experiments in the paragraphs below, along with the validated hyperparameters.

Setup for SSL Evaluation. We remark that for slide- and region-level tasks, we employ a 5-fold stratified cross-validation on the training set to find the best hyperparameters of the MIL heads. In detail, we conduct a grid search over the learning rate in $\{0.001, 0.01\}$, dropout in $\{0.2, 0.5\}$, hidden dimension of the attention in $\{128, 256\}$, and the number of layers in the classifier in $\{1, 2\}$. The hyperparameter configuration yielding the highest mean validation macro F1 score across the folds is selected, and the corresponding models are then evaluated on the held-out test set. We repeat this procedure for three MIL aggregators (ABMIL, add-ABMIL, and conj-ABMIL) and report the results of the best-performing variant in Table 2. A detailed breakdown of the performance for each individual aggregator is provided in the next section. For cell-level tasks, we use the provided train/test splits of PanNuke and NuCLS datasets and use logistic regression for non-linear probing.

Setup for SL Evaluation. For slide and region-level tasks, we employ an ACM model with an MIL head. We select the optimal hyperparameters for the GNN’s hidden dimension in $\{16, 32\}$, number of layers in $\{1, 2\}$, and hidden dimension of the attention in $\{64, 128\}$ using a stratified 5-fold cross-validation based on the highest mean validation F1 score. For cell-level tasks, we similarly use an ACM backbone with an MLP classifier on the node level and validate the GNN’s hidden dimension in $\{256, 512\}$, its number of layers in $\{3, 5\}$, and the MLP’s hidden dimension in $\{64, 128\}$ using a 2-fold and 4-fold cross-validation for PanNuke and NuCLS, respectively, given the original splits in each dataset.

Model	Number of Parameters (10^6)
DINOv2	22.01
MAE	47.58
GrpHist ($d = 512$)	9.50
GrpHist ($d = 768$)	21.12
GrpHist ($d = 1024$)	37.34

Table C.7: Model size comparison across SSL methods. We denote by d the validated embedding dimension for GrpHist models.

Pre-processing Runtimes. Table C.8 reports the average pre-processing runtime for the BACH dataset on an NVIDIA A100 GPU, illustrating the one-time overhead of dataset construction. Notably, the CPU-based steps are easily parallelizable and can be migrated to the GPU.

Stage	Device	Mean sec/patch
Cell segmentation	GPU	0.127
Cell feature extraction	CPU	0.369
Graph construction	CPU	0.009
Total pre-processing	—	0.505

Table C.8: Pre-processing runtime.

Appendix D. Additional Results

Here, we provide results from individual MIL aggregators for slide- and region-level tasks as well as additional metrics of balanced accuracy, AUROC, and AUPRC from all of the experiments mentioned in the main text. Note that the trends reported in the main text hold for these additional metrics as well.

Model	Aggregation	Datasets			
		WSI		RoI	
		TCGA-BRCA	BACH	BRACS	BreakHis
Supervised graph models					
ACM-bio	ABMIL	—	19.56 ± 5.32	11.80 ± 1.76	55.82 ± 10.33
	add-ABMIL	—	38.37 ± 2.16	21.55 ± 2.62	49.30 ± 2.53
	conj-ABMIL	—	19.63 ± 3.89	13.89 ± 4.23	53.61 ± 10.41
ACM-UNI	ABMIL	—	22.26 ± 9.08	9.62 ± 0.76	70.72 ± 6.50
	add-ABMIL	—	29.03 ± 9.92	19.95 ± 3.27	69.22 ± 8.22
	conj-ABMIL	—	24.52 ± 10.40	12.17 ± 3.57	76.27 ± 9.23
Self-supervised vision models					
DINOv2	ABMIL	62.43 ± 1.75	55.15 ± 3.28	47.88 ± 1.63	81.06 ± 4.40
	add-ABMIL	58.41 ± 4.32	59.25 ± 3.34	52.68 ± 1.78	83.44 ± 2.25
	conj-ABMIL	62.21 ± 2.54	48.95 ± 1.19	46.25 ± 2.11	82.21 ± 4.55
MAE	ABMIL	66.72 ± 1.27	53.30 ± 2.24	51.00 ± 0.93	87.02 ± 2.51
	add-ABMIL	60.65 ± 3.10	57.94 ± 3.91	56.33 ± 0.76	<u>87.74 ± 1.66</u>
	conj-ABMIL	66.35 ± 2.83	57.25 ± 3.20	50.91 ± 0.92	87.52 ± 2.19
Ours					
GrapHist	ABMIL	<u>71.40 ± 2.73</u>	69.16 ± 3.37	58.70 ± 0.97	85.84 ± 3.82
	add-ABMIL	70.17 ± 2.55	<u>68.77 ± 4.60</u>	60.30 ± 0.46	87.27 ± 4.40
	conj-ABMIL	72.25 ± 1.40	66.74 ± 2.83	<u>59.39 ± 1.89</u>	89.37 ± 1.94

Table D.9: Test macro F1 scores (%) on WSI and RoI-level breast cancer tumor subtyping tasks for all the evaluated models and aggregation methods. Best and second-best results are highlighted in bold and underlined, respectively.

Model	Aggregation	Datasets			
		WSI	RoI		
		TCGA-BRCA	BACH	BRACS	BreakHis
Supervised graph models					
ACM-bio	ABMIL	—	26.23 ± 4.41	18.69 ± 3.05	58.50 ± 8.11
	add-ABMIL	—	41.00 ± 1.40	25.16 ± 2.80	50.06 ± 2.13
	conj-ABMIL	—	24.68 ± 4.86	18.27 ± 3.10	56.89 ± 7.31
ACM-UNI	ABMIL	—	28.35 ± 6.40	11.94 ± 0.67	70.61 ± 6.11
	add-ABMIL	—	35.76 ± 8.11	26.19 ± 3.60	69.00 ± 7.96
	conj-ABMIL	—	29.17 ± 9.24	16.10 ± 3.92	75.94 ± 8.98
Self-supervised vision models					
DINOv2	ABMIL	63.06 ± 1.33	58.59 ± 2.01	49.08 ± 1.55	81.44 ± 4.25
	add-ABMIL	58.07 ± 3.79	61.65 ± 3.24	54.15 ± 1.61	83.89 ± 2.11
	conj-ABMIL	62.39 ± 2.00	50.69 ± 0.94	47.49 ± 1.72	82.17 ± 4.75
MAE	ABMIL	66.29 ± 1.37	54.19 ± 2.70	52.09 ± 0.67	87.22 ± 2.55
	add-ABMIL	60.11 ± 3.17	59.31 ± 4.56	57.20 ± 0.82	<u>87.83 ± 1.70</u>
	conj-ABMIL	66.64 ± 2.97	58.22 ± 2.92	52.06 ± 0.85	87.56 ± 2.29
Ours					
GrapHist	ABMIL	<u>71.67 ± 3.44</u>	<u>70.10 ± 3.05</u>	59.03 ± 1.43	86.06 ± 4.03
	add-ABMIL	69.85 ± 3.10	70.40 ± 3.56	60.64 ± 0.45	87.67 ± 4.54
	conj-ABMIL	72.27 ± 1.75	68.19 ± 2.32	<u>59.90 ± 2.07</u>	89.83 ± 2.36

Table D.10: Test balanced accuracy scores (%) on WSI and RoI-level breast cancer tumor subtyping tasks for all the evaluated models and aggregation methods. Best and second-best results are highlighted in bold and underlined, respectively.

Model	Aggregation	Datasets			
		WSI	RoI		
		TCGA-BRCA	BACH	BRACS	BreakHis
Supervised graph models					
ACM-bio	ABMIL	—	50.21 ± 5.22	57.13 ± 3.99	60.76 ± 8.81
	add-ABMIL	—	66.44 ± 2.58	63.08 ± 2.48	49.64 ± 4.38
	conj-ABMIL	—	46.73 ± 6.13	55.42 ± 3.16	61.98 ± 12.31
ACM-UNI	ABMIL	—	55.97 ± 5.62	47.23 ± 1.77	75.96 ± 9.25
	add-ABMIL	—	64.90 ± 5.40	62.77 ± 3.35	73.51 ± 8.48
	conj-ABMIL	—	52.69 ± 6.39	54.80 ± 8.36	79.66 ± 10.17
Self-supervised vision models					
DINOv2	ABMIL	68.80 ± 1.78	80.87 ± 1.34	83.00 ± 0.33	88.53 ± 5.16
	add-ABMIL	65.77 ± 3.04	84.38 ± 1.23	85.65 ± 0.43	91.44 ± 1.94
	conj-ABMIL	68.57 ± 2.99	76.56 ± 0.51	81.91 ± 0.90	91.19 ± 2.90
MAE	ABMIL	76.69 ± 0.66	75.11 ± 1.10	86.23 ± 0.12	93.27 ± 1.55
	add-ABMIL	66.54 ± 4.79	80.76 ± 2.48	88.98 ± 0.21	93.35 ± 1.34
	conj-ABMIL	74.49 ± 1.20	78.11 ± 0.80	86.24 ± 0.24	94.14 ± 1.13
Ours					
GrapHist	ABMIL	82.47 ± 1.72	<u>88.01 ± 1.28</u>	89.99 ± 0.31	93.64 ± 1.80
	add-ABMIL	<u>83.11 ± 1.17</u>	88.35 ± 1.39	90.78 ± 0.36	<u>94.95 ± 2.19</u>
	conj-ABMIL	84.40 ± 1.12	86.47 ± 1.05	<u>90.04 ± 0.60</u>	95.51 ± 1.60

Table D.11: Test AUROC scores (%) on WSI and RoI-level breast cancer tumor subtyping tasks for all the evaluated models and aggregation methods. Best and second-best results are highlighted in bold and underlined, respectively.

Model	Aggregation	Datasets			
		WSI	RoI		
		TCGA-BRCA	BACH	BRACS	BreakHis
Supervised graph models					
ACM-bio	ABMIL	—	30.20 ± 5.67	19.63 ± 2.77	67.43 ± 7.26
	add-ABMIL	—	42.91 ± 1.49	23.35 ± 2.35	59.13 ± 3.98
	conj-ABMIL	—	26.45 ± 3.75	17.98 ± 2.10	66.39 ± 8.75
ACM-UNI	ABMIL	—	37.60 ± 4.02	15.34 ± 0.80	76.87 ± 9.94
	add-ABMIL	—	44.35 ± 5.95	23.86 ± 2.83	73.11 ± 7.24
	conj-ABMIL	—	34.41 ± 4.75	18.78 ± 3.80	79.41 ± 10.82
Self-supervised vision models					
DINOv2	ABMIL	41.35 ± 2.87	61.10 ± 1.44	49.13 ± 0.71	90.98 ± 5.33
	add-ABMIL	38.23 ± 3.99	68.99 ± 2.74	54.81 ± 0.86	94.23 ± 1.58
	conj-ABMIL	41.13 ± 3.91	55.42 ± 1.11	48.06 ± 1.94	94.10 ± 2.57
MAE	ABMIL	51.71 ± 1.89	55.92 ± 2.55	55.37 ± 0.45	93.71 ± 2.21
	add-ABMIL	40.27 ± 5.28	64.91 ± 3.88	61.67 ± 0.53	94.22 ± 1.91
	conj-ABMIL	48.98 ± 2.32	60.59 ± 1.85	55.32 ± 0.72	95.37 ± 1.20
Ours					
GrapHist	ABMIL	<u>63.89 ± 3.83</u>	<u>74.74 ± 2.09</u>	<u>64.31 ± 1.28</u>	95.69 ± 1.32
	add-ABMIL	61.86 ± 2.66	74.93 ± 2.62	65.89 ± 1.10	<u>96.69 ± 1.50</u>
	conj-ABMIL	66.92 ± 1.75	71.66 ± 2.42	64.28 ± 1.72	96.96 ± 1.20

Table D.12: Test AUPRC scores (%) on WSI and RoI-level breast cancer tumor subtyping tasks for all the evaluated models and aggregation methods. Best and second-best results are highlighted in bold and underlined, respectively.

Model	PanNuke 20×		PanNuke 40×		NuCLS	
	Breast	PanCancer	Breast	PanCancer	main	super
Supervised graph models						
ACM-bio	<u>56.51 ± 0.41</u>	61.61 ± 0.33	56.41 ± 0.38	65.26 ± 0.59	24.68 ± 0.96	39.25 ± 1.36
ACM-UNI	57.38 ± 0.01	<u>66.72 ± 0.41</u>	<u>56.96 ± 0.19</u>	<u>65.64 ± 0.87</u>	25.29 ± 0.31	40.53 ± 1.01
Self-supervised vision models						
DINOv2	56.12 ± 0.50	60.09 ± 1.15	55.17 ± 0.57	58.91 ± 1.35	22.34 ± 1.76	41.20 ± 2.42
MAE	48.50 ± 0.86	65.25 ± 1.03	48.31 ± 0.72	65.13 ± 1.21	<u>27.47 ± 4.17</u>	<u>46.72 ± 2.89</u>
Ours						
GraphHist	56.36 ± 0.40	67.63 ± 0.68	57.49 ± 0.07	68.73 ± 0.96	28.06 ± 2.45	48.04 ± 3.14

Table D.13: Test balanced accuracy scores (%) on cell-level type identification tasks for all the evaluated models. Best and second-best results are highlighted in bold and underlined, respectively.

Model	PanNuke 20×		PanNuke 40×		NuCLS	
	Breast	PanCancer	Breast	PanCancer	main	super
Supervised graph models						
ACM-bio	81.12 ± 4.53	<u>91.07 ± 0.07</u>	82.80 ± 8.75	<u>91.48 ± 0.23</u>	75.35 ± 0.69	79.34 ± 0.43
ACM-UNI	91.39 ± 2.35	92.92 ± 0.21	89.05 ± 3.28	92.38 ± 0.09	<u>72.02 ± 0.73</u>	76.13 ± 1.16
Self-supervised vision models						
DINOv2	<u>87.58 ± 2.28</u>	84.79 ± 0.45	<u>87.36 ± 1.98</u>	84.03 ± 0.44	63.44 ± 0.52	68.09 ± 2.02
MAE	80.49 ± 4.07	86.18 ± 0.16	80.97 ± 3.47	86.17 ± 0.18	70.45 ± 3.53	75.74 ± 5.55
Ours						
GraphHist	87.09 ± 3.79	89.08 ± 0.12	85.30 ± 8.07	89.57 ± 0.05	71.49 ± 1.55	<u>77.14 ± 2.08</u>

Table D.14: Test AUROC scores (%) on cell-level type identification tasks for all the evaluated models. Best and second-best results are highlighted in bold and underlined, respectively.

Model	PanNuke 20×		PanNuke 40×		NuCLS	
	Breast	PanCancer	Breast	PanCancer	main	super
Supervised graph models						
ACM-bio	<u>61.49 ± 0.23</u>	<u>67.80 ± 0.17</u>	62.44 ± 0.02	<u>70.37 ± 0.06</u>	28.29 ± 0.46	47.78 ± 0.35
ACM-UNI	64.11 ± 0.12	73.59 ± 0.66	<u>62.40 ± 0.06</u>	72.76 ± 0.43	26.93 ± 0.44	45.20 ± 0.31
Self-supervised vision models						
DINOv2	59.52 ± 0.73	55.64 ± 1.35	58.69 ± 0.74	54.25 ± 1.17	24.63 ± 1.31	43.97 ± 2.09
MAE	50.34 ± 0.81	60.48 ± 1.35	50.09 ± 0.84	60.56 ± 1.25	<u>28.63 ± 2.07</u>	<u>49.21 ± 0.89</u>
Ours						
GraphHist	60.37 ± 0.47	65.90 ± 1.16	61.85 ± 0.30	66.30 ± 0.94	29.18 ± 1.61	49.88 ± 2.59

Table D.15: Test AUPRC scores (%) on cell-level type identification tasks for all the evaluated models. Best and second-best results are highlighted in bold and underlined, respectively.